Nano Research 2015, 8(10): 3372–3383
DOI 10.1007/s12274-015-0837-4
Research Article

ISSN 1998-0124
CN 11-5974/O4

Coherent Mn_3O_4-carbon nanocomposites with enhanced energy-storage capacitance

Chaofeng Liu[1], Huanqiao Song[1], Changkun Zhang[1], Yaguang Liu[1], Cuiping Zhang[1], Xihui Nan[1], and Guozhong Cao[1,2] (✉)

[1] *Beijing Institute of Nanoenergy and Nanosystems, Chinese Academy of Sciences, Beijing 100083, China*
[2] *Department of Materials Science and Engineering, University of Washington, Seattle, Washington 98195, USA*

Received: 23 April 2015
Revised: 5 June 2015
Accepted: 9 June 2015

KEYWORDS
sonochemical,
Mn_3O_4,
Li-on capacitor,
activated C,
nanocomposite

ABSTRACT

Nanostructured Mn_3O_4 was introduced to activated C (AC) by a novel sonochemical reaction, and the resulting nanocomposites were examined as supercapacitor electrodes. The sonication not only catalyzed the redox reaction but also promoted the diffusion of the precursors, causing the formation of coherent nanocomposites with Mn_3O_4 nanoparticles grown and uniformly distributed inside the mesopores of the AC. In addition, the extreme local condition in the sonochemical synthesis yielded an excessive amount of divalent manganese ions and oxygen vacancies. This novel microstructure endowed the sample with a superior performance, including a specific capacitance of 150 F/g compared with the value of 93 F/g for AC at a charge/discharge rate of 100 mA/g. A Li-ion capacitor delivered an energy density of 68 Wh/kg, compared with 41 Wh/kg for the AC capacitor at a power density of 210 W/kg.

1 Introduction

As electrical energy-storage devices, supercapacitors bridge the gap between conventional dielectric capacitors and batteries owing to their high energy and power densities [1, 2]. They are generally classified into two—electrical double-layer capacitors (EDLCs) and pseudo-capacitors—on the basis of the charge-storage mechanism of the electrode materials [3, 4]. EDLCs are based on the accumulation of charges at the interfaces between the electrodes and electrolytes; thus, the capacitance depends strongly on the surface area and the porous structure of the electrode materials. Pseudo-capacitors rely on a pseudo-redox reaction derived from the electron transfer between the electrode and the electrolyte. Transition-metal oxides (TMOs), carbonaceous materials decorated with functional groups, and conductive polymers are all candidates for redox reactions [2, 5, 6]. However, metal oxides and conductive polymers often exhibit a relatively poor cyclic stability and low power density, limiting their practical applications [7].

Activated C (AC) has abundant sources, a large surface area, and a good chemical stability, leading

Address correspondence to gzcao@u.washington.edu

TSINGHUA UNIVERSITY PRESS   Springer

to its wide utilization as an electrode material in supercapacitors. The surface area of AC determines the formation of the electric double layer, which dictates the speed of the pseudo-capacitive reaction. The pore size and pore morphology are also key factors affecting the electrochemical performance of AC [8]. The surface functionalization of AC plays an important role in the surface wettability and the introduction of pseudo-capacitance [9, 10]. Methods for the surface modification of AC can be categorized into three: the chemical bonding of heteroatoms [10–14], the deposition of a metal coating [15], and the incorporation of TMOs [2, 16]. As electrode materials, TMOs offer a high pseudo-capacitance through Faradaic reactions. Tailoring the microstructure and tuning the crystallinity of materials with a given chemical composition and crystal structure are effective methods for improving the electrochemical properties of TMOs and enhancing the performance of devices made of such materials [2, 7]. Combining these merits of TMOs with the large surface area and excellent electrical conductivity of carbonaceous materials has attracted considerable attention for the design and fabrication of higher-capacity electrode materials [17]. For example, the introduction of MnO_2 nanoneedles to the AC yielded an excellent electrochemical capacitance, which is attributed to the synergistic effect of both the AC porous structure and the redox reaction of the MnO_2 nanoneedles [18]. Similar results were reported for RuO_2/AC [19] and Fe_3O_4/AC [20].

To leverage the synergistic merits of both ACs and TMOs, various synthesis and processing methods have been developed and examined for the fabrication of desired nanostructures and microstructures. Sonochemical synthesis is known as an efficient, eco-friendly, and cost-effective approach for the fabrication of nanomaterials or the modification of the surface texture of materials. During the sonochemical synthesis, ultrasound can induce unique hotspots with a potential temperature above 5,000 K, pressures exceeding 1,000 bars, and heating/cooling rates above 10^{10} K/s [21]. Amorphous manganese-oxide-coated C synthesized by a sonochemical method from a mixture of $NaMnO_4$ and C delivered an initial capacity of 273 mAh/g at a charge/discharge rate of 100 mA/g in the voltage window of 1.5–4.0 V for a Li-ion battery [22]. Lee et al. adopted the sonochemical method to synthesize three-dimensional graphene/nanoparticle (NP) foam that exhibited a high specific capacitance of 421 F/g at 100 mA/g and a capacitance retention of 97% at a charge/discharge rate of 20 A/g [23]. Moreover, the localized spots with an extremely high temperature and pressure generated by the ultrasonication easily created abrupt supersaturation, yielding a high density of nucleation and subsequently uniformly sized NPs [24].

This work reports the sonochemical synthesis of coherent Mn_3O_4-AC nanocomposites and their excellent electrochemical properties as supercapacitor electrodes in an organic electrolyte. Mn_3O_4 is characterized by its high theoretical capacitance, low cost, abundance, and eco-friendliness [25]. An organic electrolyte, 1 M $LiPF_6$ in ethylene carbonate/dimethyl carbonate, was selected for its high operating voltage, which was helpful to obtain an increased energy density [26, 27]. The phases and porous structure of the resulting nanocomposites were characterized by X-ray diffractometry (XRD), scanning electron microscopy (SEM), and a nitrogen-sorption analysis. The electrochemical performances were investigated by cyclic voltammetry, galvanostatic cycling, and electrochemical impedance spectroscopy (EIS). The reaction mechanism of the sonochemical synthesis and the relationships between the processing, microstructure, and electrochemical properties of the resulting coherent Mn_3O_4-AC nanocomposite (labeled as AC-Mn) are discussed.

2 Experimental

2.1 Synthesis

A coherent trimanganese tetraoxide (Mn_3O_4)-C nanocomposite was synthesized via a sonication-assisted mechanical-stirring method using potassium permanganate ($KMnO_4$, Beijing chemical works) and AC derived from coconut shells (AC, TF-B520, Shanghai SinoTech Investment Management CO., LTD) as raw materials. First, 1.50 g of AC was dispersed into 150 mL of absolute ethyl alcohol by a mechanical stirrer and sonicated in an ultrasonic cleaning bath (720 W, 40 KHz, Kunshan, China) for 5 min. Then, 0.12 g of $KMnO_4$ was dissolved into 12 mL of deionized (DI) water.

After the pre-treatment, the AC dispersion liquid was stirred continuously and the $KMnO_4$ solution was added to it, followed by sonicated treatment for 30 min. The product was filtered and washed several times with absolute ethyl alcohol and DI water to remove the byproducts. Finally, it was dried in a vacuum oven at 150 °C for 5 h. A comparison sample was synthesized under identical conditions, except without the sonication.

2.2 Structural characterization

X-ray diffraction (XRD) analyses of the samples were conducted using a Marcogroup diffractometer (MXP21 VAHF) with a Cu-Kα radiation source (λ = 1.54056 Å). The microstructures of the samples were investigated using a cold-field emission scanning electron microscope (HITACHI SU8200) and a high-resolution transmission electron microscope (HR-TEM, Tecnai G2). The total surface area was determined by nitrogen sorption analyses using a Micromeritics surface area and porosity analyzer (ASAP 2020 HD88, USA). The degas condition was set as 250 °C for 4 h in a vacuum of 500 μm Hg (~0.67 mbar), and adsorption-desorption measurements were conducted at the temperature of liquid nitrogen. To determine the mesopore surface area, pore volume, and pore diameter, the Barrett–Joyner–Halenda (BJH) method was employed. The specific surface area and the pore volume of the micropores were calculated using the t-method. An X-ray photoelectron spectroscopy (XPS) analysis was performed using a K-Alpha 1063 instrument with a monochromatic Al Ka X-ray source operated at 72 W. The peaks of Mn2p were fitted with Gaussian–Lorentzian functions to separate the information from the two oxidation states (Mn^{2+} and Mn^{3+}). The relative atomic ratio of Mn^{2+} to Mn^{3+} was calculated according to the corresponding area ratios of these fits. The oxide content was measured using a thermogravimetric analysis (TGA)/differential thermal analysis instrument (Mettler-Toledo STAR system, TGA/SDTA) with an oxygen flow of 50 sccm/min in the temperature range of 40–800 °C at a heating rate of 10 °C/min.

2.3 Electrochemical characterization

Electrochemical tests were conducted using CR2032 coin cells assembled in an argon-filled glovebox, wherein the oxygen and water contents were both below 0.5 ppm. To prepare working electrodes, a mixture of the active material, black C, and poly-(vinyl difluoride) with a weight ratio of 80:10:10 was pasted on an Al foil. The mass loading of the active material on each electrode disk was 2.0–3.0 mg/cm^2. The electrolyte was composed of 1 M $LiPF_6$ dissolved in a mixture of ethylene carbonate/dimethyl carbonate (EC/DMC, 1:1 vol%). A cellulose film (TF4840) from NKK Corporation was used as the separator. To investigate the electrochemical properties of the electrode materials, the half cells were adopted, and lithium foil was used as the counter electrode. Furthermore, Li-ion capacitors were fabricated, in which commercial $Li_4Ti_5O_{12}$ was employed as anodes to examine the performance of different cathode materials.

Galvanostatic charge-discharge tests of the assembled cells were performed on a Land CT2001A system (Wuhan, China) at various current densities. The measured voltage range for the half cells and Li-ion capacitors were 2–4 V (vs. Li/Li^+) and 0–2.8 V (vs. $Li_4Ti_5O_{12}$), respectively. Cyclic voltammograms (CVs) were acquired using a Solartron SI 1287 electrochemical interface at a scanning rate of 0.1 mV/s. All of the electrochemical measurements were conducted at room temperature. The current densities for the half and full cells were determined according to the mass of the active materials on the cathodes. The specific energy and specific power of the full cells were calculated as follows:

$$P = \Delta V \times I / m$$

$$E = P \times t$$

$$\Delta V = (V_{\max} - V_{\min}) / 2$$

Here, I is the discharge current, t is the discharge time, m is the mass of the active materials in both electrodes, V_{max} is the potential at the beginning of the discharge after the IR drop, and V_{min} is the potential at the end of the discharge.

3 Results and discussion

Figures 1(a)–1(c) compare the XRD patterns of the AC, the sample synthesized using $KMnO_4$ and AC

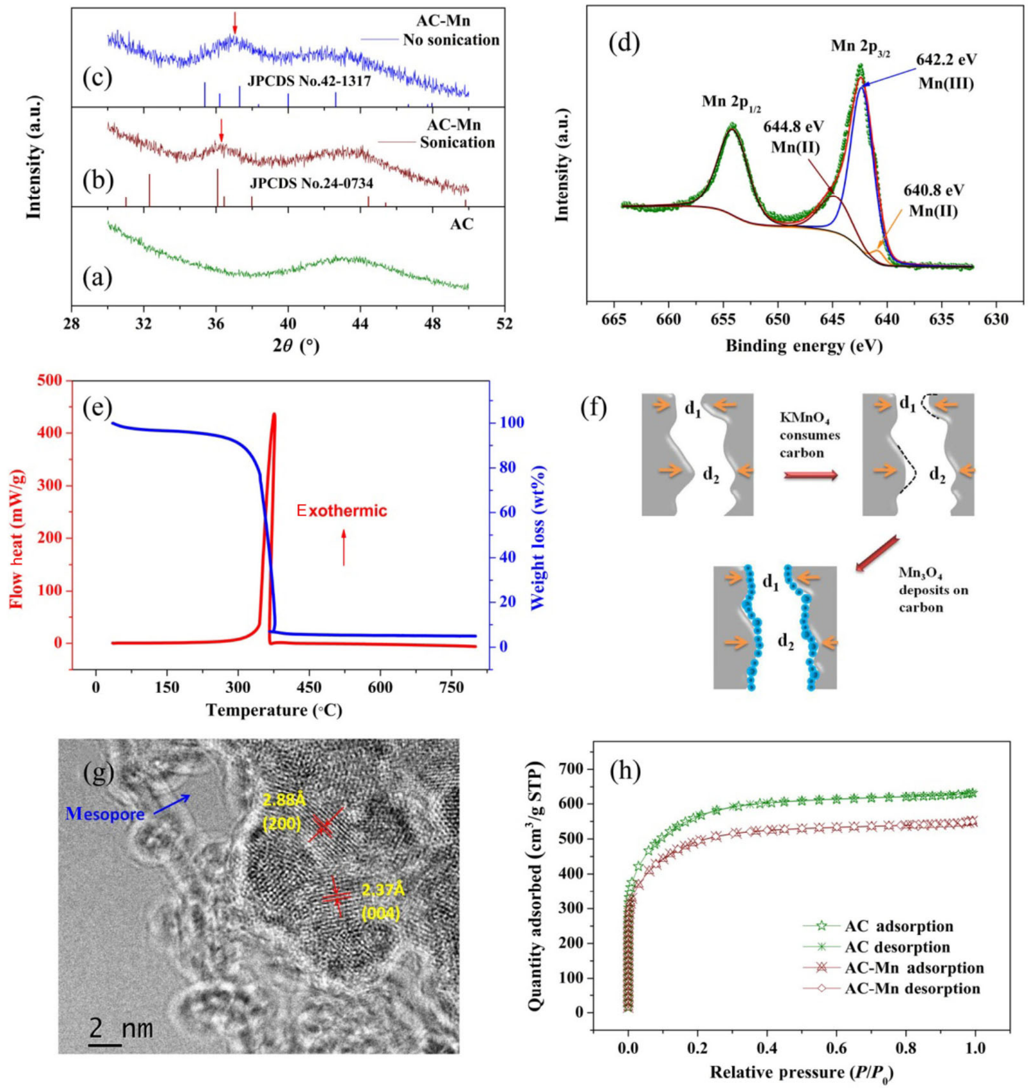

Figure 1 XRD patterns of (a) AC and (b) AC-Mn with sonication and (c) AC-Mn without sonication in the synthesis. The red arrows indicate the difference between the positions of the main peaks of the two samples. (d) XPS curves of AC-Mn with sonication; the peaks were simulated with Gaussian functions. (e) DSC/TG curves of AC-Mn sample synthesized with sonication. (f) Schematic of formation of Mn_3O_4 on AC. $KMnO_4$ reacted preferentially with pointed pores and consumes the C, yielding Mn_3O_4 deposition. (g) HR-TEM image of AC-Mn synthesized with sonication. (h) Nitrogen sorption curves of two samples; the total surface area of AC-Mn decreased compared with that of AC.

through the sonochemical reaction, and the reference sample synthesized using $KMnO_4$ and AC without sonication. The broad peak between 40° and 48° is attributed to the AC, as reported in the literature [28]. The XRD pattern (Fig. 1(b)) of the manganese-oxide-C sample obtained through the sonochemical reaction is attributed to pure Mn_3O_4 with a tetragonal structure (space group I41/amd, JCPDS card No. 24-0734). However, there is a low-intensity characteristic peak at ~36° due to the low Mn_3O_4 content of ~3.84 wt%, as well as a broad hump between 40° and 48° for C, indicating that the product is a mixture of Mn_3O_4 and C. Notably, the formation of Mn_3O_4—which is thermodynamically more favorable and stable than MnO_2—through the following reaction is commonly reported in the literature [29–31]:

$$4KMnO_4 + 3C + H_2O \rightarrow 4MnO_2 + K_2CO_3 + 2KHCO_3 \quad (1)$$

MnO_2 was formed from $KMnO_4$ and C when the reaction temperature was controlled at 73 [29] or

90 °C [30]. Our experiments confirmed the formation of MnO_2 (space group C2/m, JCPDS card No. 42-1317) from $KMnO_4$ and C without the sonication, as shown in the XRD pattern of Fig. 1(c), which agrees well with the literature [29, 30]. To ensure that the weak and broad peaks shown in Figs. 1(a)–1(c) were not mistaken as amorphous, a series of AC-Mn samples were prepared, and the distinct characteristic peaks were detected as the Mn_3O_4 content increased (Fig. S1(a) in the Electronic Supplementary Material (ESM)). An AC-Mn sample with a heavy amount of oxide comprised MnO_2 without the sonication treatment (Fig. S1(b) in the ESM). In addition, the XPS results shown in Fig. 1(d) confirm that the sample that underwent sonication comprised Mn_3O_4. The XPS spectrum revealed an increased energy separation of 11.8 eV between the $Mn2p_{1/2}$ and $Mn2p_{3/2}$ peaks. The actual metal-oxidation state in the sample was identified by fitting the XPS peaks with Gaussian functions. The $Mn2p_{3/2}$ peak was fitted by three Gaussian functions and the simulated peaks located at 640.8, 642.2, and 644.8 eV, respectively. The peak at 642.2 eV corresponds to Mn^{3+} ions, and the other two peaks correspond to Mn^{2+} ions, as widely reported in the literature [32, 33]. The ratio of Mn^{2+} to Mn^{3+} ions was estimated as 0.35 using the intensities in the area of the simulated peaks, indicating that the Mn^{2+} content was slightly higher than its stoichiometric level, which suggests the slightly excessive reduction of the raw material $KMnO_4$. According to defect chemistry and the charge-conservation law, excessive Mn^{2+} occupied the sites belonging to Mn^{3+} in stoichiometric Mn_3O_4, creating oxygen vacancies in the crystal lattice. XPS spectra of AC-Mn synthesized without sonication are shown in Fig. S2 (ESM). As shown, the energy separation was 11.7 eV between $Mn2p_{1/2}$ and $Mn2p_{3/2}$, which agrees well with the data reported in the literature [34, 35]. In addition, the energy separation related to Mn3s has been well established as 4.94 eV [36], which confirms that the AC-Mn sample synthesized without sonication comprised MnO_2. A comparison of the results for AC-Mn with and without sonication, together with the literature data, strongly suggests that the sonochemical synthesis yields a very different phase, as well as different nano- and microstructures of manganese oxides (Mn_3O_4 instead of MnO_2). Although the exact mechanism of the formation of Mn_3O_4 is a subject for further study, the extreme local reaction conditions, i.e., parameters, generated by ultrasonication are likely the causes, as briefly discussed below. In general, ultrasound does not directly interact with a reactive substance on a molecular level, because the wavelength ranges (10 to 10^{-4} cm) are far above the atomic or molecular dimensions. The sonochemical reaction arises from the result of the concentrated ultrasonic energy: the acoustic cavitation [24, 37]. The cavitation causes bubbles, and the collapse of these bubbles can generate very high local temperatures and pressures. Suslick et al. used sonoluminescence spectra to evaluate the hotspots irradiated from cavitation bubbles in various media [38, 39]. The effective hotspot temperatures are greater than 4,000 and 5,000 K in aqueous and non-aqueous media, respectively. In water, the collapse of cavitation bubbles generates a shock wave that can reach a pressure of 60,000 bars [40]. Such extreme conditions and an abrupt nature (extremely short duration) can easily alter the local thermodynamics and kinetics, promoting uncommon chemical reactions and the formation of chemicals or compounds that would otherwise not form. In addition, the ultrasonic irradiation of water or ethanol generates highly reactive radicals such as $H^{\bullet}$ and $OH^{\bullet}$ that can initiate and promote the reduction reaction [41]. Thus, the formation of Mn_3O_4 is described by the following reactions.

$$H_2O \leftrightarrow H^{\bullet} + OH^{\bullet} \tag{2}$$

$$CH_3CH_2OH \leftrightarrow CH_3CH_2O^{\bullet} + H^{\bullet} \tag{3}$$

$$MnO_2 + H^{\bullet} \rightarrow MnOOH \tag{4}$$

$$12MnOOH \rightarrow 4Mn_3O_4 + 6H_2O + O_2 \tag{5}$$

In the beginning, highly reactive $H^{\bullet}$ radicals with a reducing nature are produced by ultrasonic irradiation in water. These $H^{\bullet}$ radicals react with MnO_2 derived from $KMnO_4$ and AC to form MnOOH, and this reaction is consistent with the capacitive charge-storage mechanism of MnO_2 [42]. Finally, the extreme local conditions provide the thermodynamics for transforming MnOOH to Mn_3O_4, which is more thermodynamically stable [43]. Therefore, the slightly higher content of Mn^{2+} in the sonication product of AC-Mn, as indicated by XPS, is easily explained: highly active radicals provide an excessively reducing condition for transforming Mn^{4+} to Mn^{2+}. By tuning the solution components and sonication time, we confirmed the reducing effect of ethanol and the extreme conditions of the irradiation from the cavitation that catalyzed the chemical reactions. Thus, the optimized conditions were explored for studying coherent AC-Mn composites (Fig. S3 in the ESM). On the basis of Eq. (1), $KMnO_4$ consumes 0.47 wt% C in the initial synthesis. MnO_2 transforms into Mn_3O_4, yielding a mass loss of 12.6 wt% in the oxides. Consequently, Mn_3O_4 has a weight ratio of 3.84% in the AC-Mn sample. To further confirm the actual content of Mn_3O_4, differential scanning calorimetry (DSC) and TGA were conducted, and the results are shown in Fig. 1(e). The remaining weight ratio was 5.02%, which is higher than the result of 3.84% calculated using Eq. (1). This difference is attributed to two possible reasons. The first concerns the oxidation of Mn_3O_4 that transformed into Mn_2O_3 (Fig. S4 in the ESM) during the measurement because of the direct contact of a small amount of the sample with sufficient flowing oxygen. The second arises from the possible non-uniformity of the AC particles, which affected the loading of Mn_3O_4 with the small sample amount used in the test.

In contrast to bare AC, in the AC-Mn sample, a coating was grown and covered the C surface (Figs. S5(a) and S5(b) in the ESM). Considering that there was only 3.84 wt% of Mn_3O_4 and that Mn_3O_4 had a far higher density, the volume fraction of Mn_3O_4 was smaller than 3.84%. Thus, it was difficult to observe the morphology and distribution of Mn_3O_4 in the AC, because some of it may have been deposited on the internal surface of the mesopores of the AC. However, leaf-like matter was observed on the external surface of the AC (Fig. S5(b) in the ESM). Energy-dispersive X-ray spectroscopy was employed to confirm the composition of this material and verify it as the target product Mn_3O_4, rather than terminations or other byproducts (Figs. S5(c)–S5(e) in the ESM). The morphologies of the oxides were also determined by the synthesis conditions. The key factor, as previously mentioned, is the sonication treatment used in the synthesis, and the growth of the oxide can be explained as follows. In the beginning, ultrasound irradiation activates the surface sites of AC, and ethanol molecular adsorb on them to form reactive sites for $KMnO_4$. The radicals reduce the intermediate product from $KMnO_4$ and AC to produce Mn_3O_4, and more secondary radicals form because of the higher ethanol concentration, which yields a higher reduction rate [44]. Simultaneously, the ethanol acts as structure-directing agent to control the growth of Mn_3O_4. Thus, the higher reduction rate and limited growth direction induce the preferential nucleation of Mn_3O_4. The directing effects of ethanol for the sonochemical synthesis of metal NPs have been reported in the literature [45, 46]. To identify the morphological differences among the sonochemical samples, the samples synthesized without sonication were examined by SEM. The results, which are shown in Fig. S5(f) (ESM), indicate that the oxide was distributed randomly and the particles were irregular and non-uniform. Moreover, $KMnO_4$ contacted the surface of the AC and reacted easily with the protruding positions, such as the edges, corners, and pointedness. This is because such a convex surface has a higher surface energy and solubility than both flat and concave surfaces [47] and thus is more ready to react and more easily removed, as schematically illustrated in Fig. 1(f). Similarly, microsize pores are more favorable for the deposition of Mn_3O_4 than mesopores, as the deposition on the concave surface with a smaller radius (microsize pores) offers a greater reduction of the Gibbs free energy than the deposition inside mesopores. Thus, micropores are more likely to be obstructed by the deposition of Mn_3O_4. When sonication was applied, the shock wave generated from a collapsing bubble can reach a velocity of 4,000 m/s in water [40], allowing the transfer of the reactive ions with adequate motion energy to the internal surface of pores. Jin et al. synthesized a composite comprising MnO_2 and C nanotubes (CNTs), in which $KMnO_4$ reacts with CNTs to form MnO_2 not only on the surface defect sites, but also on the internal surface of the CNTs because a nanoscale microelectrochemical cell appeared, causing a separation between the formation sites of MnO_2 and the consumption sites of C [47]. Therefore, the shock wave supplies a propulsion for mass transportation, and the electrochemical cell ensures the charge transfer on the formation sites of the reactive materials causing Mn_3O_4 to nucleate in the internal mesopores. As shown in Fig. 2(d), the nitrogen sorption isotherms of the AC and AC-Mn samples revealed characteristics of Type I adsorption curves, indicating that the surface area ratio of the micropores was in the majority and that there was an appreciable pore-volume decrease. Table 1 shows that the BET surface area for AC-Mn—1,783.9 m^2/g—was 16.1% less than that for AC: 1,496.5 m^2/g. Additionally, the total pore volume decreased from 0.99 to 0.83 cm^3/g, exhibiting a reduction of ~16.2%; however, the pore size remained almost unchanged. Assuming that all of the Mn_3O_4 mixed with the AC mechanically, the mixture of AC with 3.84 wt% Mn_3O_4 yielded a specific surface area of 1,715.4 m^2/g (less than 4% reduction) and a pore volume of 0.95 cm^3/g (less than 4% reduction) with an unchanged pore size. The significantly larger decrease in both the specific surface area and the pore volume supports the hypothesis that the Mn_3O_4 was deposited inside the pores to incorporate SnO_2 into the CMK-3 pore channel, as previously reported [48]. Such changes arose from the complex combination of the reduction reaction of $KMnO_4$ by C with the partial removal of C and the deposition of Mn_3O_4 as shown in Fig. 1(f). The HR-TEM image shown in Fig. 1(g) supports this explanation in detail. As indicated by the blue arrow, mesopores are clearly observed in the AC. The apparent lattice fringes with an inter-planar spacing of 2.37 and 2.88 Å agree well with the planar distance between the (004) and (200) planes of Mn_3O_4, respectively, which were calculated using standard XRD data. This interface between Mn_3O_4 and the

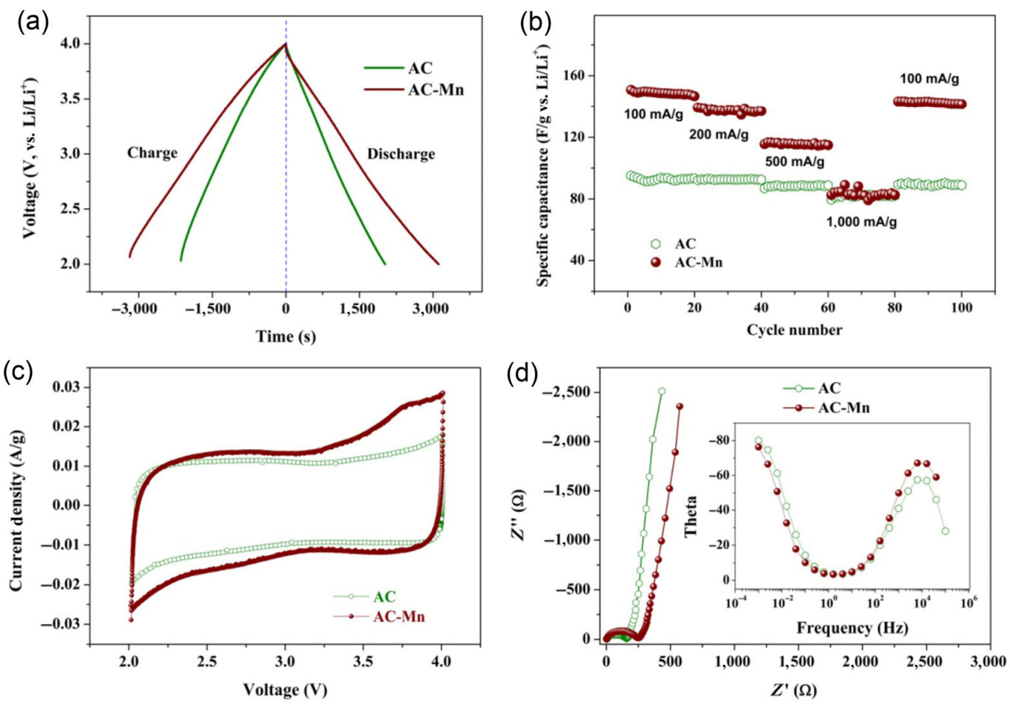

Figure 2 (a) Galvanostatic charge/discharge curves of AC and AC-Mn. (b) Specific capacitance of samples measured in the half cells, where metal lithium was used as a counter electrode. The measuring-voltage window was 2–4 V. AC-Mn exhibited better specific capacitances than AC. (c) CV curves of AC and AC-Mn samples measured at the scanning rate of 0.1 mV/s. (d) Nyquist and Bode plots for samples. The measuring-frequency range was 10^5–10^{-3} Hz, and the voltage amplitude was 10 mV.

Table 1 Specific surface area, micropore volume, and mesopore diameter of samples

Sample ID	S_{BET} ($m^2 \cdot g^{-1}$)	S_{Meso} ($m^2 \cdot g^{-1}$)	S_{Micro} ($m^2 \cdot g^{-1}$)	V_{total} ($cm^3 \cdot g^{-1}$)	V_{Meso} ($cm^3 \cdot g^{-1}$)	V_{Micro} ($cm^3 \cdot g^{-1}$)	D_{Meso} (nm)
AC	1,784	1,121	663	0.97	0.61	0.38	2.17
AC-Mn	1,497	962	535	0.83	0.52	0.31	2.17
Mixture	1,715			0.95			2.17

AC implies that the two phases formed a coherent nanocomposite.

Generally, AC is a typical EDLC material with a large surface area, whereas Mn_3O_4 exhibits pesudocapacitance owing to a redox reaction, similar to other manganese oxides. Although Mn_3O_4 has a spinel structure rather than the layer structure of MnO_2, the charge-storage reactions are very similar between the two crystals. The intercalation/chemisorption of Li^+ goes through bulk or on the surface of MnO_2 with the valence variation of Mn ions between Mn(IV) and Mn(III), as follows [42]:

$$MnO_2 + Li^+ + e^- \leftrightarrow MnOOLi \tag{6}$$

The pesudocapacitance reaction of Mn_3O_4 in an organic electrolyte is described by the following equation, which is similar to that reported in the literature for $MnO_x(OLi)_y$ [49]:

$$MnO_{1.33} + \delta Li^+ + \delta e^- \leftrightarrow MnO_{1.33}Li_\delta \tag{7}$$

The charge/discharge curve of AC-Mn exhibits a characteristic of typical EDLC electrodes (Fig. 2(a)), with an excellent specific capacitance of 150.8 F/g, which is far higher than that of AC: 95.2 F/g at 100 mA/g (Fig. 2(b)). Figure 2(c) presents the CV curves of the AC-Mn and AC samples. The AC sample exhibited the typical rectangular characteristic of EDLCs, whereas the AC-Mn sample exhibited broad oxidation peaks at 3.8 V, indicating that a redox reaction occurred in the energy-storage process. A similar effect was observed in the Cu-decorated AC sample owing to the mixed state of Cu^0–Cu^{2+}, which induced electrochemical reactions [15]. As the current densities increased, the specific capacitance of AC-Mn decreased faster than that of AC; at a current density of 1,000 mA/g, AC-Mn and AC had an almost identical specific capacitance. The specific capacitance of AC-Mn returned to its initial level when the charge current density decreased to 100 mA/g, indicating an excellent cyclic stability. The relatively rapid decrease in the capacity with an increased charge current density is attributed to the strong polarization and lower electrical conductivity of Mn_3O_4, which limited the transport process. A similar tendency was observed in other AC-Mn composites (Fig. S6 in the ESM). Nyquist plots of the EIS data for the AC-Mn and AC samples are shown in Fig. 2(d). The surface charge resistance at higher frequencies is indicated by a semicircle, and the diameter of the semicircle is larger for AC-Mn than AC. The slope of the curve at low frequencies represents the Warburg impedance, which signifies the electrolyte diffusion in the porous electrode. Both samples exhibited an almost ideal vertical line, suggesting good capacitive performance as well as similar porous structures, which corroborates the results from the nitrogen-sorption analyses. As shown in the inset, the Bode plot indicates a slight difference between the phase angles of the two curves at low frequencies. The phase angle of AC-Mn was less than that of AC at 1 mHz, indicating that AC-Mn had a higher diffusion resistance, as the angle was close to –90° standing for the ideal capacitor [50]. This high diffusion resistance is attributed to the contribution of the redox reactions [51] of Mn_3O_4, to the pesudo-capacitance. The results reveal that Mn_3O_4 can endow AC with an enhanced capacitance, particularly at low current densities. An improved capacitance and rate capability are expected when the amount of Mn_3O_4 is tailored.

Li-ion capacitors were fabricated, wherein commercial $Li_4Ti_5O_{12}$ (LTO) was adopted as anodes for its excellent rate capability and stable cycling performance [52]. The matching of the capacitance between the cathode and anode materials is required in asymmetric capacitors [50]. In the present study, the mass ratios of the cathode to the anode were calculated as 3:1 and 5:1 in AC-Mn//LTO and AC//LTO capacitors, respectively. The mass ratio is based on the charge balance of both electrodes, as follows [50]:

$$\frac{m^+}{m^-} = \frac{C^+ \times \Delta E^+}{C^- \times \Delta E^-} \tag{8}$$

where C is the specific capacitance, ΔE is the potential window during the charge/discharge process, and m is the mass of the electrode. The specific capacitance of $Li_4Ti_5O_{12}$ was measured for calculating the mass ratio of both electrodes in asymmetric capacitors (Fig. S7 in the ESM). Figure 3(a) shows the charge/discharge curves of the Li-ion capacitors, which were measured at a current density of 100 mA/g. The specific capacitance of the capacitor with the AC-Mn

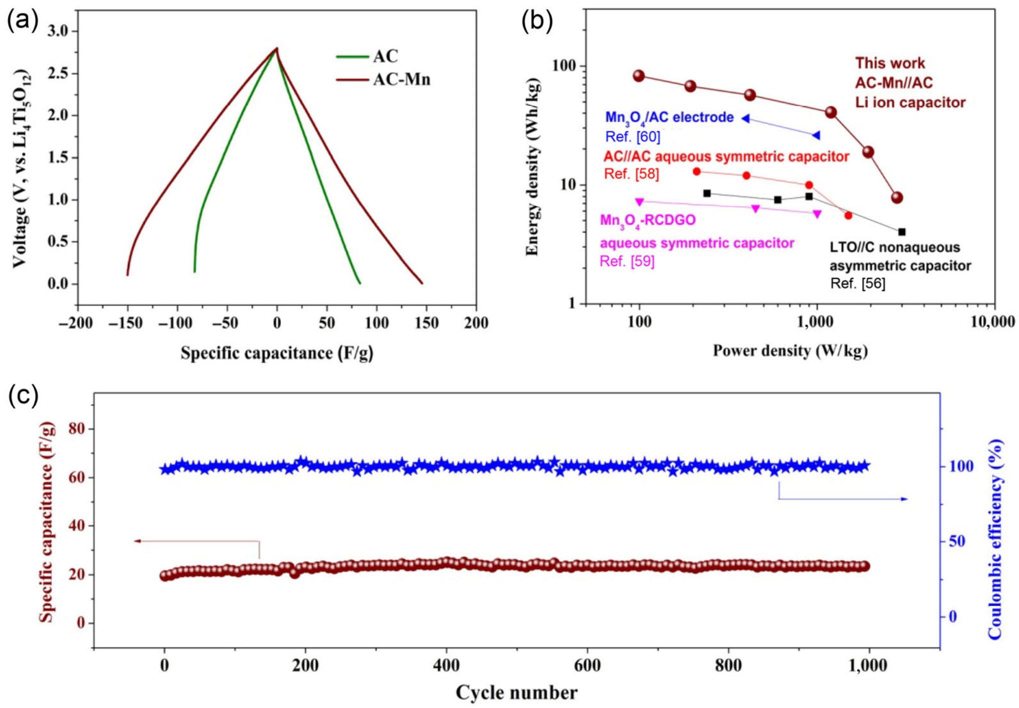

Figure 3 (a) Charge/discharge of Li-ion capacitors. AC and AC-Mn were used as cathodes, and $Li_4Ti_5O_{12}$ was used as anodes at 100 mA/g. (b) Ragone plot for Li-ion capacitors at various charge/discharge rates in the working potential range of 0–2.8 V. The data were calculated according to the total mass of the active materials on both electrodes. The performances of the capacitors based on Mn_3O_4 were collected for the parallel comparison [59, 60], indicating the favorable performance of AC-Mn//LTO. (c) Cycling performance of a Li-ion capacitor at 500 mA/g.

cathode—106 F/g—was higher than that of the AC cathode: 68 F/g. These results agree remarkably well with those measured in the half cells. The discharge curves resemble those of a typical EDLC rather than those of a pesudocapacitor, but this does not mean that the surface adsorption was the only charge-storage mechanism. Defects play an important role in the storage of ions and charges, especially in the present work. The oxygen vacancies created in the Mn_3O_4 crystal lattice provided additional active sites to accelerate the surface reactions and facilitate the phase transformation that occurred during the Li-ion insertion/extraction [53–55]. The electrochemical characteristics of compounds can be effectively tuned by introducing defects; for example, the capacitor behavior of materials becomes more dominant as the crystallite is made smaller [40] or amorphous [47], especially at the nanoscale.

The Ragone plot shown in Fig. 3(b) was obtained from charge/discharge measurements of the Li-ion capacitors at a variety of power densities based on the total mass of both electrodes. The plot summarizes and compares the electrochemical performances of the two capacitors with AC and AC-Mn as cathodes, respectively. The energy densities at a low power density, 210 W/kg, for the AC-Mn//LTO Li-ion capacitor and AC//LTO system were approximately 61 and 48 Wh/kg, respectively. At a higher power density of 1,500 W/kg, the AC//LTO hybrid capacitor exhibited an energy density of 3.9 Wh/kg, compared with the value of 3.1 Wh/kg for the AC-Mn//LTO hybrid system. This is ascribed to the fact that Mn_3O_4 on the surface of the AC did not react quickly enough to deliver charges for the storage or release of energy, which is one of the disadvantages of batteries. These specific-energy-density values for the Li-ion capacitors reveal synergistic effects compared with the literature values for EDLCs (~8.5 Wh/kg at 270 W/kg) [56, 57] or hybrid capacitors (3 Wh/kg at 1,500 W/kg) constructed by $Li_4Ti_5O_{12}$ and AC [58]. The cycling performance of the Li-ion capacitor was also tested with 1,000 cycles at 500 mA/g, and no appreciable degradation was observed, as shown in Fig. 3(c). This indicates that the coherent Mn_3O_4 has an excellent cycling stability as an electrode material. The aforementioned results reveal that the coherent Mn_3O_4-AC nanocomposite has an improved specific capacitance and considerable energy densities. Combining the merits of battery materials with EDLC C materials provides a reliable method to enhance the performance of the cathode materials in Li-ion capacitors.

4 Conclusions

A facile, eco-friendly, and low-cost method was investigated for synthesizing a superior capacitive material: a coherent Mn_3O_4-AC nanocomposite with an excellent specific capacitance of 106 F/g and energy density of 68 Wh/kg in a Li-ion full capacitor without device optimization. Superior properties were derived from the effective merits of the combination of AC and Mn_3O_4. This combination are attributed to the sonochemical method, which provides extreme local conditions to anchor nanostructured Mn_3O_4 in the wall of the mesopores and external surface of the AC. The extreme local conditions in the sonochemical synthesis yielded an excessive amount of divalent manganese ions and oxygen vacancies, promoting the electrochemical reactions. The higher voltage window of the organic system and higher capacitance of AC-Mn contributed to the realization of the novel devices with improved energy and power densities.

Acknowledgements

This work was supported by the "Thousands Talents" Program for Pioneer Researcher and His Innovation Team, China. This work was also supported by the National Natural Science Foundation of China (No.51374029), Program for New Century Excellent Talents in University (No. NCET-13-0668), Fundamental Research Funds for the Central Universities (No. FRF-TP-14-008C1) and China Postdoctoral Science Foundation (No. 2014M550675).

Electronic Supplementary Material: Supplementary material (XRD patterns related to phase evolution of manganese oxides with various amount of $KMnO_4$, solution and sonication time. XPS of AC-Mn sample synthesized without sonication. Elements mapping of AC-Mn sample, electrochemical performances of $Li_4Ti_5O_{12}$.) is available in the online version of this article at http://dx.doi.org/10.1007/s12274-015-0837-4.

References

[1] Yan, J.; Wang, Q.; Wei, T.; Fan, Z. Recent advances in design and fabrication of electrochemical supercapacitors with high energy densities. *Adv. Energy Mater.* **2014**, *4*, 1300816.

[2] Augustyn, V.; Simon, P.; Dunn, B. Pseudocapacitive oxide materials for high-rate electrochemical energy storage. *Energy Environ. Sci.* **2014**, *7*, 1597–1614.

[3] Zhang, Q. F.; Uchaker, E.; Candelaria, S. L.; Cao, G. Z. Nanomaterials for energy conversion and storage. *Chem. Soc. Rev.* **2013**, *42*, 3127–3171.

[4] Hall, P. J.; Mirzaeian, M.; Fletcher, S. I.; Sillars, F. B.; Rennie, A. J. R.; Shitta-Bey, G. O.; Wilson, G.; Cruden, A.; Carter, R. Energy storage in electrochemical capacitors: designing functional materials to improve performance. *Energy Environ. Sci.* **2010**, *3*, 1238–1251.

[5] Yuan, L. Y.; Yao, B.; Hu, B.; Huo, K. F.; Chen, W.; Zhou, J. Polypyrrole-coated paper for flexible solid-state energy storage. *Energy Environ. Sci.* **2013**, *6*, 470–476.

[6] Candelaria, S. L.; Garcia, B. B.; Liu, D. W.; Cao, G. Z. Nitrogen modification of highly porous carbon for improved supercapacitor performance. *J. Mater. Chem.* **2012**, *22*, 9884–9889.

[7] Wei, W. F.; Cui, X. W.; Chen, W. X.; Ivey, D. G. Manganese oxide-based materials as electrochemical supercapacitor electrodes. *Chem. Soc. Rev.* **2011**, *40*, 1697–1721.

[8] Sevilla, M.; Mokaya, R. Energy storage applications of activated carbons: supercapacitors and hydrogen storage. *Energy Environ. Sci.* **2014**, *7*, 1250.

[9] Zhou, Y.; Candelaria, S. L.; Liu, Q.; Huang, Y. X.; Uchaker, E.; Cao, G. Z. Sulfur-rich carbon cryogels for supercapacitors with improved conductivity and wettability. *J. Mater. Chem. A* **2014**, *2*, 8472–8482.

[10] Hulicova-Jurcakova, D.; Puziy, A. M.; Poddubnaya, O. I.; Suarez-Garcia, F.; Tascon, J. M. D.; Lu, G. Q. Highly stable performance of supercapacitors from phosphorus–enriched carbons. *J. Am. Chem. Soc.* **2009**, *131*, 5026–5027.

[11] Garcia, B. B.; Candelaria, S. L.; Cao, G. Z. Nitrogenated porous carbon electrodes for supercapacitors. *J Mater. Sci.* **2012**, *47*, 5996–6004.

[12] Huang, Y. X.; Candelaria, S. L.; Li, Y. W.; Li, Z. M.; Tian,

J. J.; Zhang, L. L.; Cao, G. Z. Sulfurized activated carbon for high energy density supercapacitors. *J.Power Sources* **2014**, *252*, 90–97.

[13] Milczarek, G.; Ciszewski, A.; Stepniak, I. Oxygen-doped activated carbon fiber cloth as electrode material for electrochemical capacitor. *J. Power Sources* **2011**, *196*, 7882–7885.

[14] Wang, D. W.; Li, F.; Chen, Z. G.; Lu, G. Q.; Cheng, H. M. Synthesis and electrochemical property of boron-doped mesoporous carbon in supercapacitor. *Chem. Mater.* **2008**, *20*, 7195–7200.

[15] Zhang, L. L.; Candelaria, S. L.; Tian, J. J.; Li, Y.; Huang, Y.-X.; Cao, G. Z. Copper nanocrystal modified activated carbon for supercapacitors with enhanced volumetric energy and power density. *J. Power Sources* **2013**, *236*, 215–223.

[16] Kim, M.; Hwang, Y.; Min, K.; Kim, J. Introduction of MnO_2 nanoneedles to activated carbon to fabricate high-performance electrodes as electrochemical supercapacitors. *Electrochim. Acta* **2013**, *113*, 322–331.

[17] Zhi, M.; Xiang, C.; Li, J.; Li, M.; Wu, N. Nanostructured carbon-metal oxide composite electrodes for supercapacitors: a review. *Nanoscale* **2013**, *5*, 72–88.

[18] Kim, M.; Hwang, Y.; Min, K.; Kim, J. Introduction of MnO_2 nanoneedles to activated carbon to fabricate high-performance electrodes as electrochemical supercapacitors. *Electrochim. Acta* **2013**, *113*, 322–331.

[19] Zhang, J. R.; Jiang, D. C.; Chen, B.; Zhu, J. J.; Jiang, L. P.; Fang, H. Q. Preparation and electrochemistry of hydrous ruthenium oxide/active carbon electrode materials for supercapacitor. *J. Electrochem. Soc* **2001**, *148*, A1362–A1367.

[20] Wang, Y.; He, P.; Zhao, X.; Lei, W.; Dong, F. Coal tar residues-based nanostructured activated carbon/Fe_3O_4 composite electrode materials for supercapacitors. *J. Solid State Electr.* **2014**, *18*, 665–672.

[21] Xu, H.; Zeiger, B. W.; Suslick, K. S. Sonochemical synthesis of nanomaterials. *Chem. Soc. Rev.* **2013**, *42*, 2555–2567.

[22] Kawaoka, H.; Hibino, M.; Zhou, H.; Honma, I. Sonochemical synthesis of amorphous manganese oxide coated on carbon and application to high power battery. *J. Power Sources* **2004**, *125*, 85–89.

[23] Lee, K. G.; Jeong, J.-M.; Lee, S. J.; Yeom, B.; Lee, M.-K.; Choi, B. G. Sonochemical-assisted synthesis of 3D graphene/nanoparticle foams and their application in supercapacitor. *Ultrason. Sonochem.* **2015**, *22*, 422–428.

[24] Xu, H. X.; Zeiger, B. W.; Suslick, K. S. Sonochemical synthesis of nanomaterials. *Chem. Soc. Rev.* **2013**, *42*, 2555–2567.

[25] Brock, S. L.; Duan, N.; Tian, Z. R.; Giraldo, O.; Zhou, H.; Suib, S. L. A Review of porous manganese oxide materials. *Chem. Mater.* **1998**, *10*, 2619–2628.

[26] Aurbach, D.; Talyosef, Y.; Markovsky, B.; Markevich, E.; Zinigrad, E.; Asraf, L.; Gnanaraj, J. S.; Kim, H.-J. Design of electrolyte solutions for Li and Li-ion batteries: a review. *Electrochim. Acta* **2004**, *50*, 247–254.

[27] Leng, K.; Zhang, F.; Zhang, L.; Zhang, T. F.; Wu, Y. P.; Lu, Y. H.; Huang, Y.; Chen, Y. S. Graphene-based Li-ion hybrid supercapacitors with ultrahigh performance. *Nano Res.* **2013**, *6*, 581–592.

[28] Smith, J. W. H.; McDonald, M.; Romero, J. V.; MacDonald, L.; Lee, J. R.; Dahn, J. R. Small and wide angle X-ray studies of impregnated activated carbons. *Carbon* **2014**, *75*, 420–431.

[29] Lee, S.-W.; Bak, S.-M.; Lee, C.-W.; Jaye, C.; Fischer, D. A.; Kim, B.-K.; Yang, X.-Q.; Nam, K.-W.; Kim, K.-B. Structural changes in reduced graphene oxide upon MnO_2 deposition by the redox reaction between carbon and permanganate ions. *J. Phys. Chem. C* **2014**, *118*, 2834–2843.

[30] Jia, X.; Yan, C.; Chen, Z.; Wang, R.; Zhang, Q.; Guo, L.; Wei, F.; Lu, Y. Direct growth of flexible $LiMn_2O_4$/CNT lithium-ion cathodes. *Chem. Commun.* **2011**, *47*, 9669–9671.

[31] Peng, Y. T.; Chen, Z.; Wen, J.; Xiao, Q. F.; Weng, D.; He, S. Y.; Geng, H.; Lu, Y. Hierarchical manganese oxide/carbon nanocomposites for supercapacitor electrodes. *Nano Res.* **2011**, *4*, 216–225.

[32] Dong, R.; Ye, Q.; Kuang, L.; Lu, X.; Zhang, Y.; Zhang, X.; Tan, G.; Wen, Y.; Wang, F. Enhanced supercapacitor performance of Mn_3O_4 nanocrystals by doping transition-metal ions. *ACS Appl. Mater. Inter.* **2013**, *5*, 9508–9516.

[33] Lee, J. W.; Hall, A. S.; Kim, J.–D.; Mallouk, T. E. A Facile and template-free hydrothermal synthesis of Mn_3O_4 nanorods on graphene sheets for supercapacitor electrodes with long cycle stability. *Chem. Mater.* **2012**, *24*, 1158–1164.

[34] Li, Z. P.; Mi, Y. Q.; Liu, X. H.; Liu, S.; Yang, S. R.; Wang, J. Q. Flexible graphene/MnO_2 composite papers for supercapacitor electrodes. *J. Mater. Chem.* **2011**, *21*, 14706–14711.

[35] Yan, J.; Fan, Z. J.; Wei, T.; Cheng, J.; Shao, B.; Wang, K.; Song, L. P.; Zhang, M. L. Carbon nanotube/MnO_2 composites synthesized by microwave-assisted method for supercapacitors with high power and energy densities. *J. Power Sources* **2009**, *194*, 1202–1207.

[36] Wang, J.-G.; Yang, Y.; Huang, Z.-H.; Kang, F. Y. A high-performance asymmetric supercapacitor based on carbon and carbon–MnO_2 nanofiber electrodes. *Carbon* **2013**, *61*, 190–199.

[37] Shchukin, D. G.; Radziuk, D.; Möhwald, H. Ultrasonic fabrication of metallic nanomaterials and nanoalloys. *Annu. Rev. Mater. Res.* **2010**, *40*, 345–362.

[38] Didenko, Y. T.; McNamara, W. B.; Suslick, K. S. Hot spot

conditions during cavitation in water. *J. Am. Chem. Soc.* **1999**, *121*, 5817–5818.

[39] Flint, E. B.; Suslick, K. S. The temperature of cavitation. *Science* **1991**, *253*, 1397–1399.

[40] Ohl, C. D.; Kurz, T.; Geisler, R.; Lindau, O.; Lauterborn, W. Bubble dynamics, shock waves and sonoluminescence. *Philos. Trans. R Soc. Lond. Ser. A–Math. Phys. Eng. Sci.* **1999**, *357*, 269–294.

[41] Vinodgopal, K.; Neppolian, B.; Lightcap, I. V.; Grieser, F.; Ashokkumar, M.; Kamat, P. V. Sonolytic design of graphene−Au nanocomposites. Simultaneous and sequential reduction of graphene oxide and Au(III). *J. Phys. Chem. Lett.* **2010**, *1*, 1987–1993.

[42] Wei, W.; Cui, X.; Chen, W.; Ivey, D. G. Manganese oxide-based materials as electrochemical supercapacitor electrodes. *Chem. Soc. Rev.* **2011**, *40*, 1697–1721.

[43] Yan, D.; Yan, P. X.; Cheng, S.; Chen, J. T.; Zhuo, R. F.; Feng, J. J.; Zhang, G. A. Fabrication, in-depth characterization, and formation mechanism of crystalline porous birnessite MnO_2 film with amorphous bottom layers by hydrothermal method. *Cryst. Growth. Des.* **2009**, *9*, 218–222.

[44] Caruso, R. A.; Ashokkumar, M.; Grieser, F. Sonochemical formation of gold sols. *Langmuir* **2002**, *18*, 7831–7836.

[45] Zhang, J. L.; Du, J. M.; Han, B. X.; Liu, Z. M.; Jiang, T.; Zhang, Z. F. Sonochemical formation of single-crystalline gold nanobelts. *Angew. Chem.* **2006**, *118*, 1134–1137.

[46] Jiang, L.-P.; Xu, S.; Zhu, J.-M.; Zhang, J.–R.; Zhu, J.-J.; Chen, H.-Y. Ultrasonic-assisted synthesis of monodisperse single-crystalline silver nanoplates and gold nanorings. *Inorg. Chem.* **2004**, *43*, 5877–5883.

[47] Jin, X.; Zhou, W.; Zhang, S.; Chen, G. Z. Nanoscale micro-electrochemical cells on carbon nanotubes. *Small* **2007**, *3*, 1513–1517.

[48] Qiao, H.; Li, J.; Fu, J. P.; Kumar, D.; Wei, Q. F.; Cai, Y. B.; Huang, F. L. Sonochemical synthesis of ordered SnO_2/CMK-3 nanocomposites and their lithium storage Properties. *ACS Appl. Mater. Inter.* **2011**, *3*, 3704–3708.

[49] Wu, M.; Snook, G. A.; Chen, G. Z.; Fray, D. J. Redox deposition of manganese oxide on graphite for supercapacitors. *Electrochem. Commun.* **2004**, *6*, 499–504.

[50] Chang, J.; Jin, M. H.; Yao, F.; Kim, T. H.; Le, V. T.; Yue, H. Y.; Gunes, F.; Li, B.; Ghosh, A.; Xie, S. S. et al. Asymmetric supercapacitors based on graphene/MnO_2 nano-spheres and graphene/MoO_3 nanosheets with high energy density. *Adv. Funct. Mater.* **2013**, *23*, 5074–5083.

[51] Garcia, B. B.; Candelaria, S. L.; Liu, D.; Sepheri, S.; Cruz, J. A.; Cao, G. High performance high-purity sol-gel derived carbon supercapacitors from renewable sources. *Renewable Energy* **2011**, *36*, 1788–1794.

[52] Brousse, T.; Marchand, R.; Taberna, P. L.; Simon, P. TiO_2 (B)/activated carbon non–aqueous hybrid system for energy storage. *J. Power Sources* **2006**, *158*, 571–577.

[53] Kang, B.; Ceder, G. Battery materials for ultrafast charging and discharging. *Nature* **2009**, *458*, 190–193.

[54] Hahn, B. P.; Long, J. W.; Mansour, A. N.; Pettigrew, K. A.; Osofsky, M. S.; Rolison, D. R. Electrochemical Li-ion storage in defect spinel iron oxides: The critical role of cation vacancies. *Energy Environ. Sci.* **2011**, *4*, 1495-1502.

[55] Liu, D. W.; Liu, Y. Y.; Garcia, B. B.; Zhang, Q. F.; Pan, A. Q.; Jeong, Y.-H.; Cao, G. Z. V_2O_5 xerogel electrodes with much enhanced lithium-ion intercalation properties with N_2 annealing. *J. Mater. Chem.* **2009**, *19*, 8789–8795.

[56] Ruiz, V.; Blanco, C.; Santamaría, R.; Ramos-Fernández, J. M.; Martínez-Escandell, M.; Sepúlveda-Escribano, A.; Rodríguez-Reinoso, F. An activated carbon monolith as an electrode material for supercapacitors. *Carbon* **2009**, *47*, 195–200.

[57] Xing, W.; Huang, C. C.; Zhuo, S. P.; Yuan, X.; Wang, G. Q.; Hulicova–Jurcakova, D.; Yan, Z. F.; Lu, G. Q. Hierarchical porous carbons with high performance for supercapacitor electrodes. *Carbon* **2009**, *47*, 1715–1722.

[58] Du Pasquier, A.; Plitz, I.; Menocal, S.; Amatucci, G. A comparative study of Li-ion battery, supercapacitor and nonaqueous asymmetric hybrid devices for automotive applications. *J. Power Sources* **2003**, 115, 171–178.

[59] Gao, F.; Qu, J.; Zhao, Z.; Zhou, Q.; Li, B.; Qiu, J. A green strategy for the synthesis of graphene supported Mn_3O_4 nanocomposites from graphitized coal and their supercapacitor application. *Carbon* **2014**, *80*, 640–650.

[60] Nagamuthu, S.; Vijayakumar, S.; Muralidharan, G. Synthesis of Mn_3O_4/amorphous carbon nanoparticles as electrode material for high performance supercapacitor applications. *Energy & Fuels* **2013**, *27*, 3508–3515.